



## Analytical Modeling and Evaluation of Microneedles Apparatus with Deformable Soft Tissues for Biomedical Applications

Apichart Boonma<sup>1</sup>, Roger J. Narayan<sup>2</sup> and Yuan- Shin Lee<sup>3</sup>

<sup>1</sup>Industrial and Systems Engineering, North Carolina State University, [aboonma@ncsu.edu](mailto:aboonma@ncsu.edu)

<sup>2</sup>Biomedical Engineering, North Carolina State University, [rjnaraya@ncsu.edu](mailto:rjnaraya@ncsu.edu)

<sup>3</sup>Industrial and Systems Engineering, North Carolina State University, [yslee@ncsu.edu](mailto:yslee@ncsu.edu)

### ABSTRACT

This paper presents an analytical modeling of microneedle insertion force to evaluate different microneedle geometric designs. To analyze the microneedle insertion force, monotonous and heterogeneous tetrahedral models of soft tissue were developed. This paper introduces a two-stage analytical modeling technique by considering different geometric design parameters. The method divides microneedle insertion process into pre-puncture and post-puncture stages, and employs the concept of finite element analysis, fracture mechanics and distributed load. Different microneedle designs can be evaluated based on the geometric design parameters. Experiments were conducted with both the linear elastic and the nonlinear finite element models. The microneedle geometry that provides better tissue penetration and operation stability is selected and used for biomedical applications. The presented techniques can be used in the design and development of microneedles for biomedical applications.

Keywords: biomedical device design, soft tissue modeling, geometry analysis.

DOI: 10.3722/cadaps.2013.139- 157

### 1 INTRODUCTION

Microneedles hold great potentials to be used in various medical applications such as drug delivery, local cell treatment, bio- sampling, control- released, and etc. Since microneedles are typically small in size, they are very likely to have structural failure under external loads. Microneedle experiences various kinds of external loads e.g. axial and transversal load especially during the insertion and removal from the soft tissue [1]. Skin properties contribute greatly to the forces that microneedles experience. Human skin acts as a barrier to prevent all kinds of physical and chemical damages to the inner organs. The skin consists of three major layers including Stratum Corneum, Epidermis, and

Dermis [2]. Among them the Stratum Corneum is the toughest with Young's modulus  $\sim 1$  GPa, while Young's modulus of Epidermis and Dermis are 0.134 and 0.08 MPa respectively.

Fig. 1 shows an example of microneedle array fabricated and developed in the authors' earlier work presented in [1]. The puncture point of a microneedle can be determined using the concept of fracture mechanics. Modeling of needle insertion has been achieved in the past by applying similar method [3,4,5,6]. In the theory, at the puncture point the energy equation yields balance between the work created by needle displacement and the summation of internal strain energy and the energy required to initiate the crack. Typically fracture mechanics must be applied under certain conditions i.e., assuming that soft tissue fracture is under quasi static state (happen infinitely slow) and can be described by fracture model (tensile stress perpendicular to plane of crack). Besides being employed in cutting force modeling, the concept was applied in insertion analysis of microneedle although the internal strain energy and friction term were not appear in the model [7]. Azar et al later modified the energy equation by adding a friction term [8]. However, the work was based on needle insertion of standard bevel needle in mesoscale.

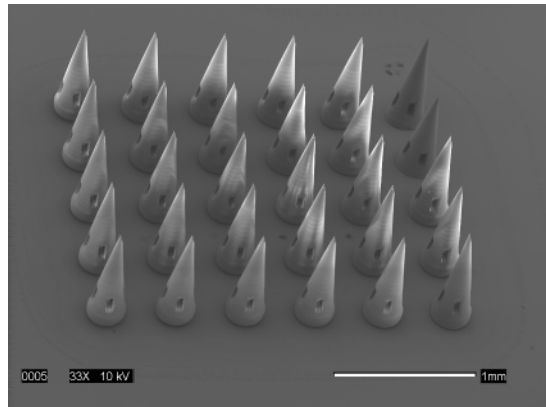


Fig. 1: Microneedle array fabricated for biomedical applications [1].

In our earlier works, a study on the medical surgical cutting on soft tissues was conducted and presented in [9,10]. Effect of microneedle geometry on the forces was previously studied in part [1,7,9,10]. The previous researchers discovered that the insertion force increases linearly with the interfacial area. The interfacial area is the interface between microneedle and skin during insertion. However, thorough studies on the effect of geometric parameters have been inadequate as most work considered only interfacial area, length, and diameter of microneedles. Tip angle was mostly left out and its effects to insertion force of microneedle remain unclear. Given the skin properties and a number of microneedle geometries to choose from, we are interested in developing an analytical method that may help to select the proper microneedle for biomedical applications.

In this paper, we present a nonlinear finite element technique to model interaction between microneedle and soft tissue during pre-puncture stage, and to predict the insertion force. Our objective is to develop a technique that can be used to define puncture point of the given microneedles

and to predict the insertion forces during pre- and post-puncture state. The presented technique is based on fracture mechanics, finite element analysis, and distributed load. Details of the two-stage techniques of microneedles are presented in the following sections.

## 2 PRE-PUNCTURE FORCE MODELING AND PUNCTURE POINT DETERMINATION

### 2.1 Nonlinear finite element modeling for soft tissue deformation

Human skin consists of three primary tissue layers including Stratum Corneum, Epidermis, and Dermis [1,2]. As shown in Fig. 2, the Stratum Corneum is the outermost skin with the thickness of approximately 10 - 40  $\mu\text{m}$  [12]. Epidermis lies in the middle between Stratum Corneum and Dermis with the thickness of 75 - 150  $\mu\text{m}$ . The inner most layer is the Dermis that is about 1 - 2 mm thick and contains blood vessels, sweat glands, hair follicles and nerve endings that provide sense of touch and heat. Therefore, if a microneedle does not penetrate deeply into Dermis layer, it is guaranteed that the process is pain-free. Our tissue model was developed based on this information on skin thickness.

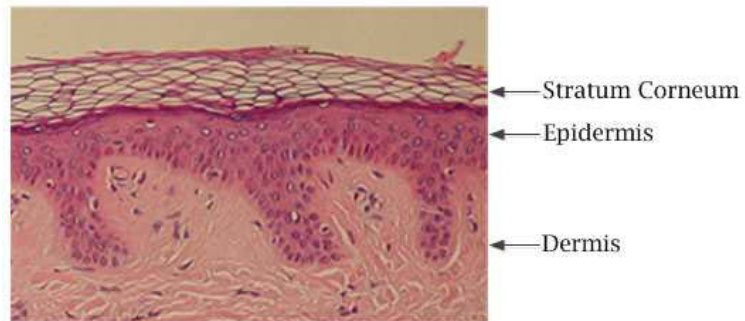


Fig. 2: Example of anatomy of human skin [12].

In our earlier works, soft tissue modeling and the soft tissue properties were studied and presented in [1,9,10]. In this paper, we create a soft tissue model of skin that consists of four-node tetrahedrons. Each tetrahedron is linked with four neighboring tetrahedron (if exist). A tetrahedron comprises of four triangle faces that can be defined by switching orders of the nodes. This data structure is crucial for maintaining correct topology of the model and suitable for fast retrieval of tetrahedron information. Although the accuracy of tetrahedral model is less than that provided by hexahedral model, it is more versatile and suitable for complex geometries transitioning from coarsely to finely meshed volume [11]. Lastly, the tissue properties represented by Young's modulus and Poisson ratio are assigned to each tetrahedron.

Microneedle is created as a solid object at first and then discretized into triangular meshed model, similar to a solid model with stereolithography format (STL). Fig. 3 shows an example of convex hull of flat tip cylinder microneedle and contact tetrahedrons which are equivalent to contact nodes. Once the contact nodes are defined, tissue deformation engine powered by a nonlinear finite element method can be employed.

Soft tissue demonstrates a nonlinear- pseudo- elastic property. We formulate the nonlinear model by establishing a nonlinear relationship between strain and displacement, where a second degree polynomial function is applied. An element strain/displacement function can be written in the classic form as follows:

$$\epsilon_x = \frac{\partial u}{\partial x} + \frac{1}{2} \left[ \left( \frac{\partial u}{\partial x} \right)^2 + \left( \frac{\partial v}{\partial x} \right)^2 + \left( \frac{\partial w}{\partial x} \right)^2 \right] \tag{1}$$

And shear strain can be formulated in Equation (2). Similar expression can be applied for shear strain in other directions as well.

$$\gamma_{xy} = \frac{\partial u}{\partial y} + \frac{\partial v}{\partial x} + \frac{\partial u}{\partial y} \frac{\partial u}{\partial x} + \frac{\partial v}{\partial y} \frac{\partial v}{\partial x} + \frac{\partial w}{\partial y} \frac{\partial w}{\partial x} \tag{2}$$

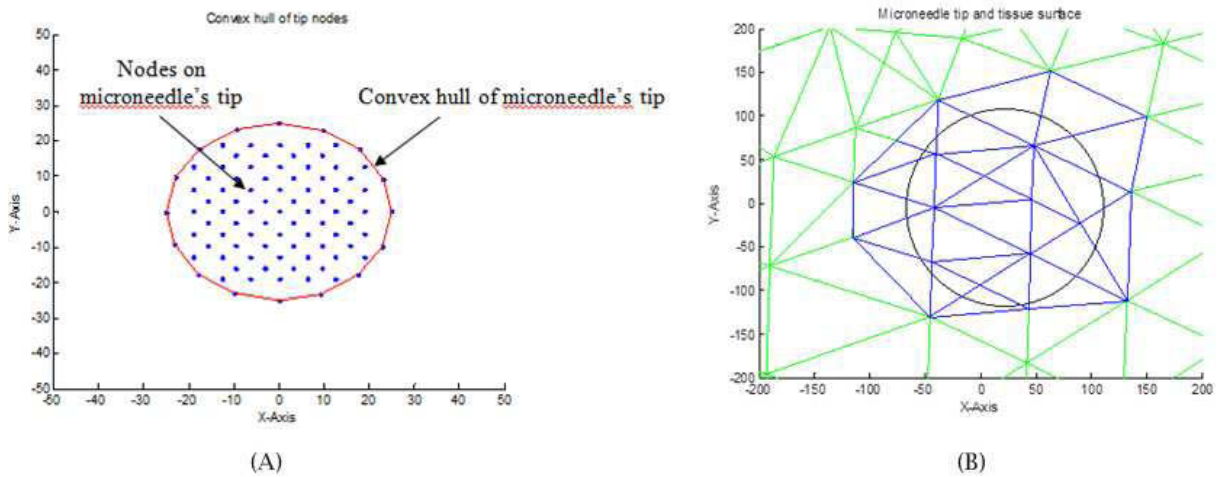


Fig. 3: (A) Example of convex hull of a cylinder microneedle and (B) contact nodes found after mapping the convex hull onto tissue surface.

The stress  $[\sigma_x \sigma_y \sigma_z \tau_{xy} \tau_{yz} \tau_{zx}]^T$  and strain elements  $[\epsilon_x \epsilon_y \epsilon_z \gamma_{xy} \gamma_{yz} \gamma_{zx}]^T$  are assumed to have a linear relationship between them i.e.  $\sigma = D\epsilon$ , where  $D$  is called constitutive matrix and can be computed from the following:

$$D = \frac{EG}{(1+\nu)(1-2\nu)} \tag{3}$$

where  $E$  is the Young's modulus,  $\nu$  is the Poisson ratio, and

$$G = \begin{bmatrix} 1-\nu & \nu & \nu & & & \\ \nu & 1-\nu & \nu & & & \\ \nu & \nu & 1-\nu & & & \\ & & & 0.5-\nu & & \\ & & & & 0.5-\nu & \\ & & & & & 0.5-\nu \end{bmatrix} \tag{4}$$

The stiffness matrix  $K$  of a tetrahedral element can be obtained from:

$$K = B^T DBV = \frac{EV}{(1+\nu)(1-\nu)} B^T GB \quad (5)$$

where  $B$  is a matrix relative to the position of the elements, and  $V$  is the volume of an element. The nonlinear strain/displacement makes the internal force dependent to nodal displacement ( $u(x,y,z)$ ). The force can be formulated as:

$$F = K \cdot u + g(u) \cdot u \quad (6)$$

Equation (6) is based on quasi- static state. We postulate that there is no acceleration and the needle is moving at constant pace. To describe how to solve Equation (6), we rewrite the equation in full form and obtain:

$$\begin{bmatrix} F_n \\ F_c \end{bmatrix} = \begin{bmatrix} k_{11} & k_{12} \\ k_{21} & k_{22} \end{bmatrix} \begin{bmatrix} u_n \\ u_c \end{bmatrix} + g(u) \begin{bmatrix} u_n \\ u_c \end{bmatrix} \quad (7)$$

where  $u_n$  and  $u_c$  is the displacement at non- contact and contact nodes respectively.  $F_n$  and  $F_c$  represent force at non- contact and contact nodes. The unknowns here are the displacements at non- contact nodes and the force at contact nodes. Equation (7) can be extracted further and yield:

$$F_n = k_{11}u_n + k_{12}u_c + g(u) \cdot u_n \quad (8)$$

$$F_c = k_{21}u_n + k_{22}u_c + g(u) \cdot u_c \quad (9)$$

Since  $F_n$  is zero and  $u_c$  is known, we can determine  $u_n$  by using Equation (8). Substitute all known variables into the equation and we eventually obtain

$$k_{11}u_n + g(u) \cdot u_n = -k_{12}u_c \quad (10)$$

Solve Equation (10) for  $u_n$  then substitute  $u_n$  and  $u_c$  into Equation (9) and the force  $F_c$  at contact node can be computed. Equations (8), (9), and (10) cannot be easily solved [13]. In this paper, an iterative method is developed to find the solutions. Details are presented in the following sections.

## 2.2 Energy tracking method for determining microneedle puncture points

When microneedles cutting into soft tissue, the cutting force of microneedle can be predicted by interchange of energy between the work created by microneedle, the work for creating the cut, and the internal strain energy due to deformation. The governing energy model may be formulated by the following Equation (3) shown as follows:

$$Fdx + dU = JdA + d\Delta + d\tau + dR \quad (11)$$

where  $F$  is the force acting on the microneedle and  $dx$  is microneedle displacement.  $dU$  is the strain energy stored in the tissue.  $J$  is the resistance to fracture or sometimes called fracture toughness. Considering Equation (11), the strain energy  $dU$  stored in the tissue is ignored as the tissue not being pre- stressed. The term  $d\tau$  become zero as well due to the assumption that the soft tissue will regain its original shape after removal of microneedle. Lastly the friction term  $dR$  can be ignored since, at the

puncture point, microneedle just initiates the crack and there is no friction just yet. Based on these observations, Equation (11) can be reduced to:

$$Fdx = JdA + d\Delta \tag{12}$$

That is, the force at puncture can be determined by the size of the crack and the deformation of soft tissue at the time. The fracture toughness  $J$  can be computed from experimental data. A microneedle was inserted into the same spot twice. In the first time, Equation (12) is still valid as all the terms contribute to the process. In the second time that the needle was pushed though the skin, Equation (12) must be modified as there is no energy related to initiate the crack in the tissue anymore (since the tissue was already cracked in the first cut). The modified function is formulated as the following:

$$F'dx = d\Delta \tag{13}$$

By substituting Equation (13) into (12), the following can be found:

$$J = \frac{(F-F')dx}{dA} \tag{14}$$

Equation (14) shows the fracture toughness  $J$  can be computed from the function between insertion force of both insertion passes and the area of the crack. Fig. 4(a) shows the relationship between insertion force and displacement of two insertion tests at the same spot. In Fig. 4(A), the lower curve indicates the insertion force during the microneedle penetration. Fig. 4(B) shows the relationship between  $(F - F')dx$  and  $dA$ . By using Equation (4), the value of  $J$  is found to be 0.019 N/mm.

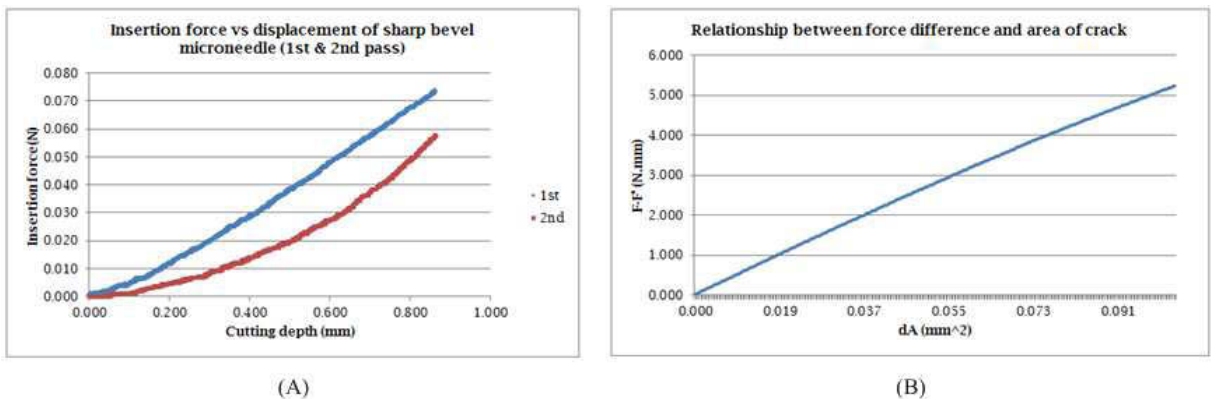


Fig. 4: (A) Relationship between insertion force and displacement by a sharp bevel microneedle. (B) Relationship between  $(F - F')dx$  and  $dA$  on a silicone rubber material.

Puncture point is where the force on the tissue is larger than the tissue rupture force [5]. Considering Equation (12), pressure over the cracking area can be computed by dividing the equation with  $(dAdx)$ , and thus can find the following:

$$\frac{F}{dA} = \frac{J}{dx} + \frac{d\Delta}{dAdx} \tag{15}$$

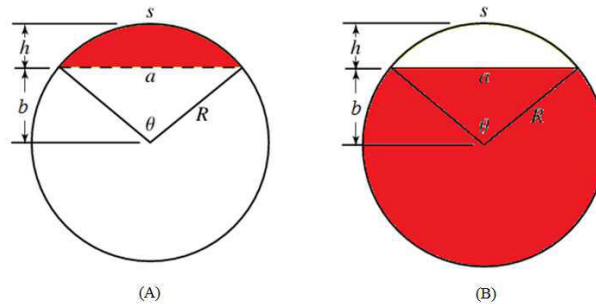


Fig. 5: Geometric parameters used in calculating tip area of a bevel microneedle.

In Equation (15), the cracking area  $dA$  is computed from the area of circular segment (this is specific to a bevel microneedle) and  $dA = (R^2 \cos^{-1} \frac{b}{R} - b\sqrt{R^2 - b^2})$  for a sharp bevel needle; and  $dA = (\pi R^2 - R^2 \cos^{-1} \frac{b}{R} - b\sqrt{R^2 - b^2})$  for a blunt bevel needle. The description of  $b$  and  $R$  can be found in Fig. 5. The strain energy  $d\Delta$  is computed from  $(\frac{1}{2}u^T Ku)$  where  $u$  is displacement matrix and  $K$  is the stiffness matrix. Substitute all the expressions into Equation (15), one can find the following for sharp bevel microneedle:

$$P_s = \frac{F}{A} = \frac{J}{dx} + \frac{\frac{1}{2}u^T Ku}{R^2 \cos^{-1} \frac{b}{R} - b\sqrt{R^2 - b^2}} \quad (16)$$

And, the equation for blunt bevel microneedle becomes:

$$P_b = \frac{F}{A} = \frac{J}{dx} + \frac{\frac{1}{2}u^T Ku}{\pi R^2 - R^2 \cos^{-1} \frac{b}{R} - b\sqrt{R^2 - b^2}} \quad (17)$$

From Equations (16) and (17), puncturation is reached when the pressure on the soft tissue underneath the microneedle ( $P_s, P_b$ ) exceeds the critical pressure of the material ( $P_c$ ), which can be obtained from the experiment. Once the pre-puncture force is reached, the modeling shifts into the post-puncture force modeling. Details of the post-puncture force analysis are discussed in the following sections.

### 3 POST-PUNCTURE INSERTION FORCE MODELING

Post-puncture insertion force is crucial for deciding whether a needle can reach the target depth. In this paper, we use the distributed load to predict the forces exert to a microneedle. During insertion, microneedle pushes soft tissue away from original position. We postulate that microneedle is moved along the longitudinal axis and the direction that soft tissue is displaced is in the direction perpendicular to the surface of microneedle. It is also assumed that microneedle is subjected to different types of distributed loads during insertion process depending on its geometry. The insertion force is generated due to the displacement of soft tissue when it is replaced by the microneedle. To define these triangles, we categorize all the triangles on the microneedle into the following groups based on their normal vectors and insertion direction: (i) Group\_1 with triangle whose normal points perpendicularly to inserting direction; (ii) Group\_2 with triangle whose normal points to similar

direction as inserting direction; and Group\_3 with triangle whose normal points to opposite direction as inserting direction. Fig. 6 shows these different types of triangles on microneedle models.

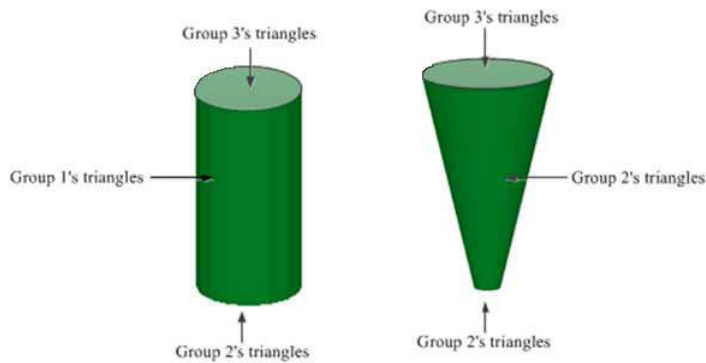


Fig. 6: Modeling of microneedle geometries.

To model the microneedle insertion force, we first subdivide the microneedle surface into two sub-types:  $\alpha$  and  $\beta$ . As shown in Fig. 7,  $\alpha$ -triangles are those whose normal vectors are exactly in similar direction to insertion direction (cross product of the two vectors is close to zero). An example of  $\alpha$ -triangles is a triangle on the tip of blunt or cone shape needles.  $\beta$ -triangles, on the other hand, are those whose normal vectors are deviated from the insertion direction but still points toward the insertion path (dot product of the two vectors yields positive value). An example of  $\beta$ -triangles is a triangle on the slope portion of cone shape needles as shown in Fig. 7.

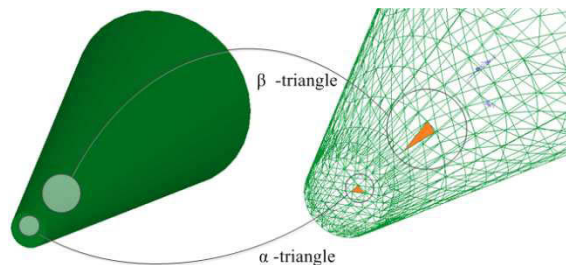


Fig. 7: Example of  $\alpha$ -triangles and  $\beta$ -triangles in cone tip microneedle.

During the insertion process, given that the surface of the tip is perpendicular to the insertion direction and the tip of microneedle is always pressed against the skin, the  $\alpha$ -triangles lying on the tip will be subjected to uniformly distributed load across their surface area. In the meantime, the  $\beta$ -triangles located on the sloped body of the needle will cause triangular distributed load. This can be portrayed by Fig. 8, where round and blunt tip cone-shaped needles are shown on the left and right respectively.

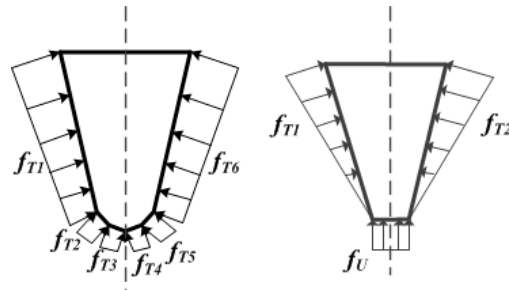


Fig. 8: Insertion force distribution on the  $\alpha$ - triangles and  $\beta$ - triangles.

Insertion force on  $\alpha$ - triangle can be represented by a concentrated load  $F_U$  which is a computation of uniformly distributed load  $f_U$ .  $F_U$  can be computed as a load with magnitude equal to multiplication of the constant force and the area under load. The general expression for resultant of uniformly distributed load is given as:

$$F_{U,i} = KS \sum_{i=1}^n A_i \quad (18)$$

where  $K$  is the stiffness of the skin per unit length of the needle,  $S$  is a scale constant defined from the experiment,  $A_i$  is area of an  $\alpha$ - triangle  $i$ ,  $n$  is total number of  $\alpha$ - triangles at the area under uniform load. Similar to the case of  $\alpha$ - triangle, insertion force on a  $\beta$ - triangle can be computed from the volume of the load over the area of the triangle. The difference, however, is that the distributed load over a  $\beta$ - triangle is in a form of triangularly distributed load. This type of distributed load is dependent to location of the three vertices and distance to the needle's tip. Computation of the resulting force representing the triangularly distributed load can be divided into three cases according to these factors, as shown in Fig. 9. In Fig. 9(A), only one vertex of  $\beta$ - triangle is located at the tip of the needle. In Fig. 9(B), two vertices of  $\beta$ - triangle are located at the tip of the needle. In Fig. 9(C), none of the vertices is located at the tip of the needle.

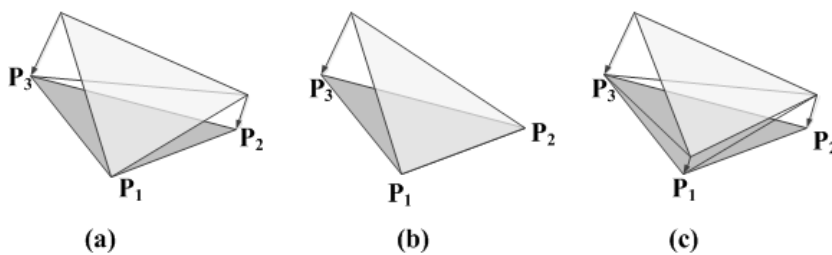


Fig. 9: Different cases in computing distributed load on  $\beta$ - triangle.

To compute triangularly distributed load over a  $\beta$ - triangle, we first compute the distributed load on each vertex of the triangle. Considering a  $\beta$ - triangle  $i$  consisting of three vertices  $P_1$ ,  $P_2$ , and  $P_3$  as shown in Fig. 10, if vertex  $P_2$  is not on the needle's tip (the distributed load is not zero), the load  $f_T(P_2)$  at vertex  $P_2$  can be computed by the following procedure:

Step\_1: Compute two points ( $O_1, O_2$ ) on the center axis of the needle.

Step\_2: Compute centroid  $CG_i$  of  $\beta$ - triangle  $i$ .

Step\_3: Create a reference plane from  $O_1, O_2$ , and  $CG_i$ .

Step\_4: Project  $P_1, P_2$  and  $P_3$  onto the reference plane and find the projected points  $Q_1, Q_2$  and  $Q_3$ .

Step\_5: Compute the angle  $\theta$  between the center axis  $\overline{O_1O_2}$  and  $\overline{Q_1Q_2}$  as shown in Fig. 10.

Step\_6: The distributed load at  $P_1, P_2$  and  $P_3$  can be computed by using the following formulations:

$$\begin{aligned}
 f_T(P_1) &= 0 && ; P_1 \text{ is on the needle's tip} \\
 f_T(P_1) &= f_T(Q_1) = KS\left(\frac{b}{\cos\left(\frac{\theta_{Q_2} + \theta_{Q_3}}{2}\right)}\right) && ; P_1 \text{ is not on the needle's tip} \\
 f_T(P_2) &= f_T(Q_2) = KS\left(a \tan \theta_{Q_2} + \frac{b}{\cos \theta_{Q_2}}\right) && ; P_2 \text{ is not on the needle's tip} \\
 f_T(P_3) &= f_T(Q_3) = KS\left(a \tan \theta_{Q_3} + \frac{b}{\cos \theta_{Q_3}}\right) && ; P_3 \text{ is not on the needle's tip}
 \end{aligned}$$

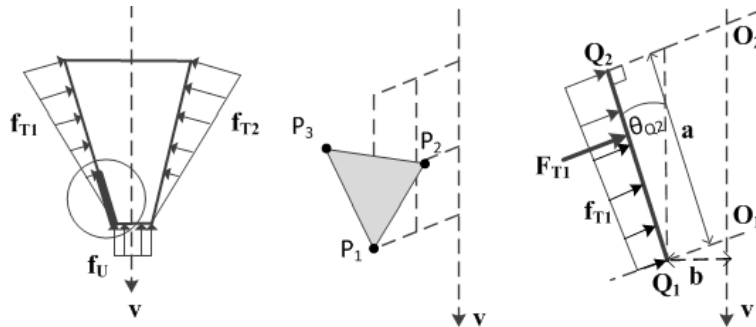


Fig. 10: Force diagram of a triangular element ( $\beta$ - triangle) and the method used to compute the distributed load at each vertex.

The distributed load on the three vertices could become either one of the three cases (see Fig. 9) that we have described earlier. The volume of a tetrahedron can be computed from its four vertices  $P_1, P_2, P_3$ , and  $P_4$  as shown by follows.

$$V = \frac{1}{6} |(P_1 - P_4) \cdot ((P_2 - P_4) \times (P_3 - P_4))| \quad (19)$$

And the total volume of pentahedron which is equal to the concentrated load on the triangle can be obtained from:

$$F_T = \sum_{i=1}^n V_i \quad (20)$$

The presented techniques were developed as algorithms and implemented into a software program. Fig. 11 shows the flowchart of the algorithm of determining the insertion force and puncture point.

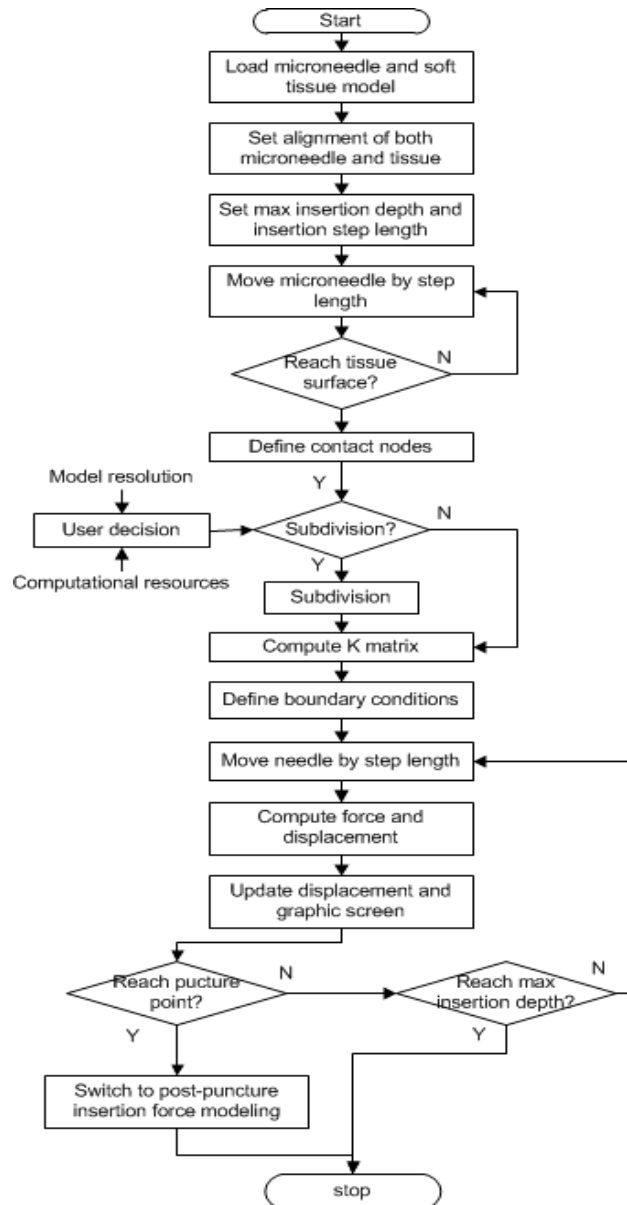


Fig. 11: Overview of the algorithm for the insertion force computation.

#### 4 EXPERIMENTS AND RESULTS

The proposed two-stage modeling technique was implemented at North Carolina State University on an Intel® CORE™ i3 CPU laptop loaded with Intel® HD graphics, 4GB of RAM, and Microsoft Windows 7 64 bit. An example soft tissue model was first built as solid sample filled with monotonous material e.g. silicone rubber for validation purpose. Properties of the rubber are represented by Young's modulus and Poisson ratio of 0.2 MPa and 0.48 - 0.49 respectively. The soft tissue model was later

extended to assume heterogeneous properties of soft tissue consisting of three layers: Stratum Corneum, Epidermis, and Dermis. Their Young's moduli were set to 1 GPa, 0.134 MPa, and 0.08 MPa respectively [14, 15]. All tissue layers had the Poisson ratio of 0.4. Soft tissue model had the dimension of  $3000 \times 3000 \times 1150 \mu\text{m}$ . It was first built as a solid object using SolidWorks and converted to tetrahedral meshed model using Gmsh [16].

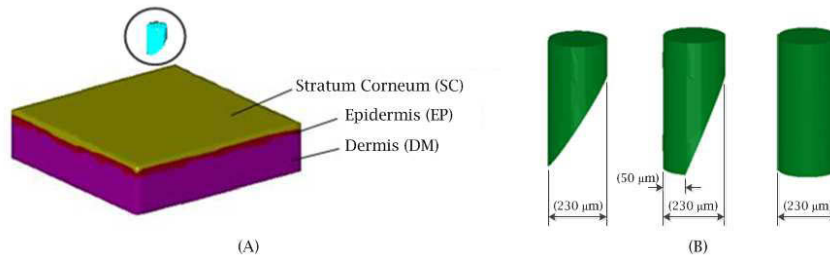


Fig. 12. (A) Heterogeneous soft tissue model. (B) Sharp bevel, blunt bevel, and cylindrical microneedles.

Three computer models of solid microneedles were built, as shown in Fig. 12. They assumed the shape of sharp bevel, blunt bevel and cylindrical microneedle. All microneedles had base diameter and length of 230 and 1000  $\mu\text{m}$  respectively. The needles were considered as solid objects represented by triangular meshes. Fig. 12(A) and 12(B) show the example of heterogeneous soft tissue model and the microneedle geometries used in this study.

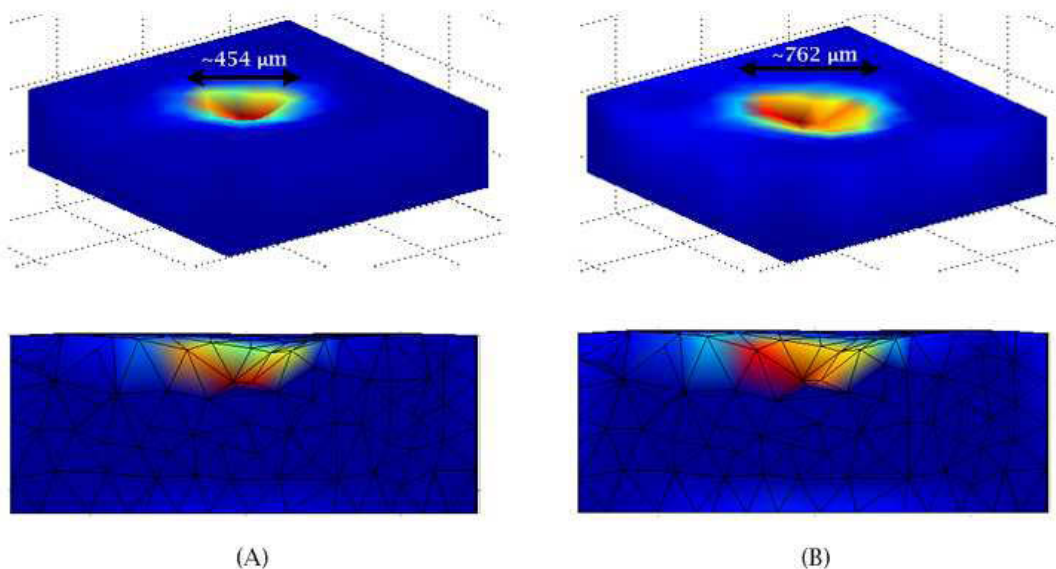


Fig. 13. Stress on soft tissue (A) by sharp bevel microneedle; (B) by blunt bevel microneedle.

In the pre-puncture phase, a microneedle starts at rest position then moves toward the soft tissue. Deformation of soft tissue occurs after microneedle contacts the tissue surface. Fig. 13 shows an example of soft tissue deformation and stress concentration around the insertion point when a

microneedle was inserted at the depth of 200  $\mu\text{m}$ . As expected the deformation is concentrated around the insertion point and gradually faded away due to the nonlinearity of soft tissue. Fig. 13(a) shows stress concentration of sharp bevel microneedle while Fig. 13(b) displays the stress caused by blunt bevel microneedle. Stress concentrated at smaller area as in the case of sharp bevel microneedle provides successful puncture at shorter insertion depth. This is confirmed by experimental data shown later in this section.

Fig. 14 shows the stress concentration map on the soft tissue model after a patch of four microneedles were inserted on the example soft tissue. Each microneedle was positioned at each corner of the tissue and about 1600  $\mu\text{m}$  apart from each other. All microneedles were moved until they reached the insertion depth of 200  $\mu\text{m}$ . High stress was detected around the area of insert and near the boundary of the tissue model. This is due to the preset boundary condition that no tissue nodes on the boundary faces are moveable.

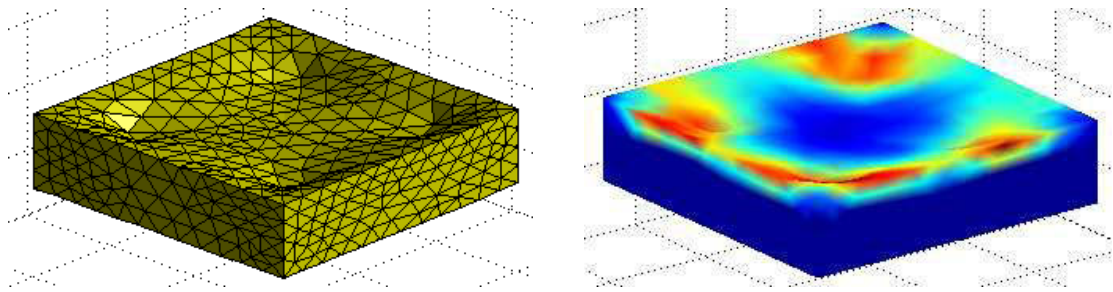


Fig. 14: Deformation of soft tissue and stress concentration around insertion sites of four microneedles at insertion depth of 200  $\mu\text{m}$ .

Fig. 15(A) shows deformation of soft tissue with Young's modulus of 0.2 MPa (Silicone rubber). Fig. 15(B) shows deformation of human skin where the Stratum Corneum (outermost layer) has the Young's modulus of 1 GPa. Deformation of soft tissue with high Young's modulus is rather shallow but covers large area. Soft tissue with low Young's modulus, on the other hand, has deeper deformation but the severity is confined at small area. Fig. 15 demonstrates this phenomenon.

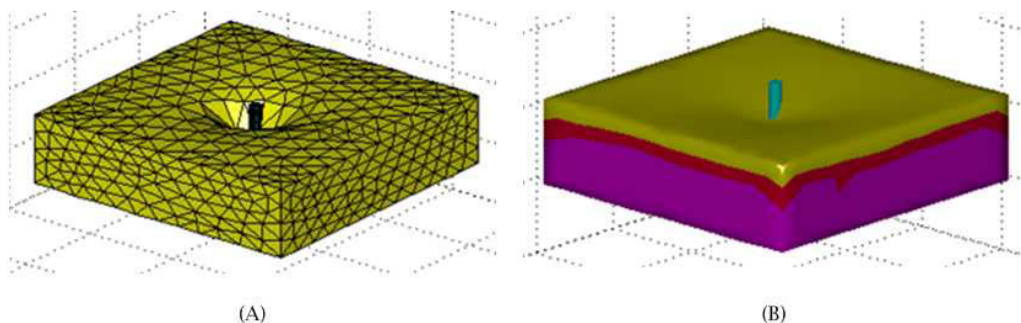


Fig. 15: Deformation of soft tissue with different Young's modulus. (A) Young's modulus is 0.2 MPa. (B) Young's modulus at top, middle, bottom layers are 1 GPa, 0.134 MPa, and 0.08 MPa respectively.

Fig. 16 shows an example of puncture point by a sharp bevel microneedle. For silicone rubber, it was found that the sharp bevel microneedle can easily puncture into the material. The insertion depth of less than 20  $\mu\text{m}$  was sufficient to create a pressure larger than the critical pressure (which is about 0.663 MPa on the average). A blunt bevel microneedle made a successful puncture at the insertion depth further than 250  $\mu\text{m}$ . This is more than 10 times of the required insertion depth of the sharp bevel microneedle. And a cylinder microneedle was found to puncture at the insertion depth larger than 500  $\mu\text{m}$ .

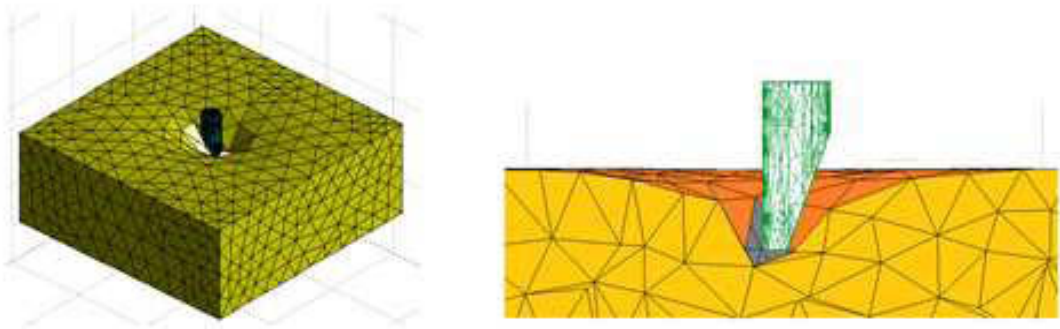


Fig. 16: Profile of sharp bevel microneedle and soft tissue at puncture point.

Fig. 17 shows a predicted insertion force when tissue property changes. With Young’s modulus of 0.2 and 0.5 MPa, and tissue phantom which has the following dimension: diameter = 44.107 mm, height = 21.145 mm, tissue toughness of  $1.043 \times 10^{-7}$  and  $2.607 \times 10^{-7}$  can be achieved. As shown in Fig. 17, for an application where a blunt microneedle needs to penetrate into soft tissue phantom further than 300  $\mu\text{m}$  (for bio- sampling, the microneedle must penetrate into human skin deeper than 700  $\mu\text{m}$ ), microneedle must be strong enough to withstand the force of 0.14 N. Therefore a microneedle that cannot resist this load should not be selected for the application. This is an example on how the insertion force model is used to pre- screening the microneedles. The technique can also be applied to various soft tissue properties.

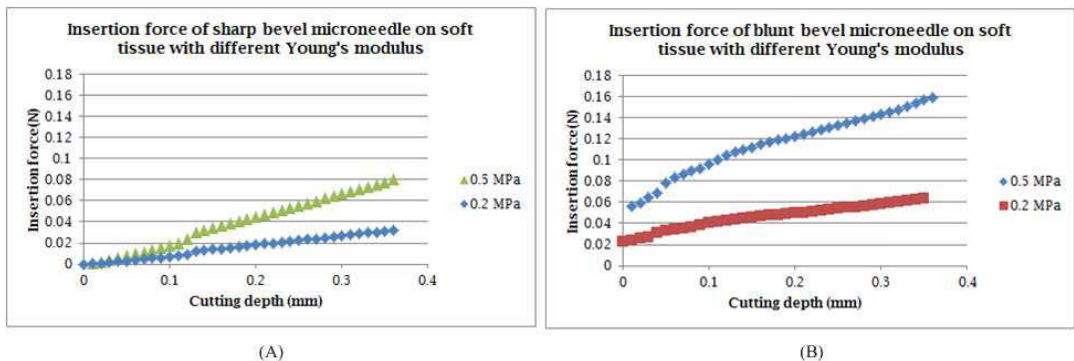


Fig. 17: The predicted insertion force of (A) sharp bevel microneedle and (B) blunt bevel microneedle when Young’s modulus changes from 0.2 MPa to 0.5 MPa.

To investigate insertion force created by microneedles of different geometries, a number of experiments were conducted. Fig. 18 shows different needle geometries used in the experiments. As shown in Fig. 18, sharp bevel, blunt bevel and cylindrical needles were used in the experiments. All needles were fabricated out of silicon, with internal and external diameter of about 90 and 230  $\mu\text{m}$  respectively. The flat area on the blunt bevel needle is approximately 50  $\mu\text{m}$  wide. The tissue phantom was made from translucent silicone rubber (Mold Max<sup>®</sup> 10T). Young's modulus of this silicone rubber is approximately 29 psi (0.2 MPa). While Young's modulus of human stratum corneum, epidermis, and dermis are 1 GPa, 0.134 MPa, and 0.08 MPa respectively, the silicone rubber positions itself slightly above the epidermis. For each set of experiment, the needle and tissue phantom were mounted onto the ElectroForce<sup>®</sup> 3100 test instrument as shown in Fig. 19. In the experiment, the needle was slowly driven toward the tissue phantom at a constant speed until it reached the maximum needle displacement of 1 mm for sharp bevel needle and 2 mm for blunt bevel and cylindrical needle.

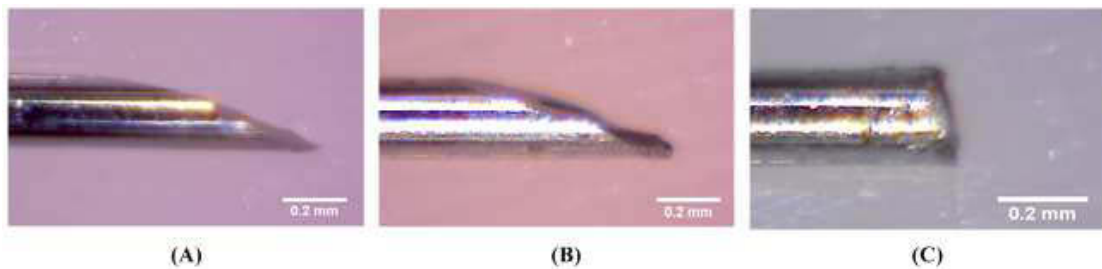


Fig. 18: Three different needle tip used in the experiments: (A) sharp bevel tip needle, (B) blunt bevel tip needle, (C) cylindrical needle.

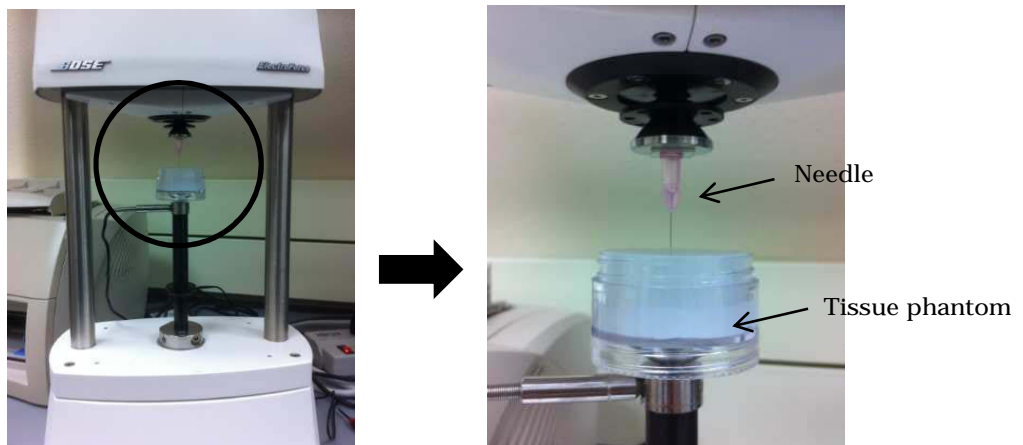


Fig. 19: ElectroForce<sup>®</sup> 3100 test instrument with a needle and tissue phantom mounted on it.

Fig. 20 shows different insertion forces relative to insertion depth of all three microneedles used in our experiments. From the observation of experiments, once microneedle touched the tissue phantom, the insertion force increased with the increase of insertion depth. As expected, a sharp bevel needle encounters a much less insertion force, while a cylinder needle causes the largest insertion force, as

shown in Fig. 20. The blunt tip and the cylinder tip microneedles encountered higher penetration resistance, but once the microneedles penetrated the tissue, the resistance force dropped slightly, as shown in Fig. 20. For the sharp bevel needle, it reached the maximum distance with much less resistance from the tissue and rapidly reached the maximum depth of insertion. In fig. 20, we believe that the drop in force resistance after microneedle insertion could be due to the relaxation of tissue phantom. Similar phenomenon in needle insertion into liver had been reported earlier [17].

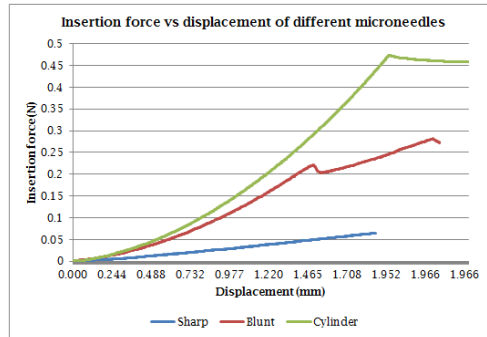


Fig. 20: Different insertion force relative to insertion depth of sharp, blunt bevel microneedle, and cylinder microneedle.

Sharp and blunt bevel microneedles reached puncture point at approximately 0.23 mm and 1.226 mm respectively. These puncture point were achieved with insertion force of 0.014 N and 0.217 N with average critical pressure of 0.663 MPa at the tip. Fig. 21 shows puncture point of sharp and blunt bevel microneedle. There was no puncture point for cylinder needle as it didn't penetrate the tissue phantom within 2 mm of needle displacement. From the data, sharp needle can penetrate into the tissue phantom quite easily compared to other needles. Although blunt needle can also reach the puncture point, it needs to traverse four times more than the sharp needle and thus causes more deformation to the tissue phantom. Also, the relationship between the force and insertion depth appeared to change from second degree polynomial to linear.

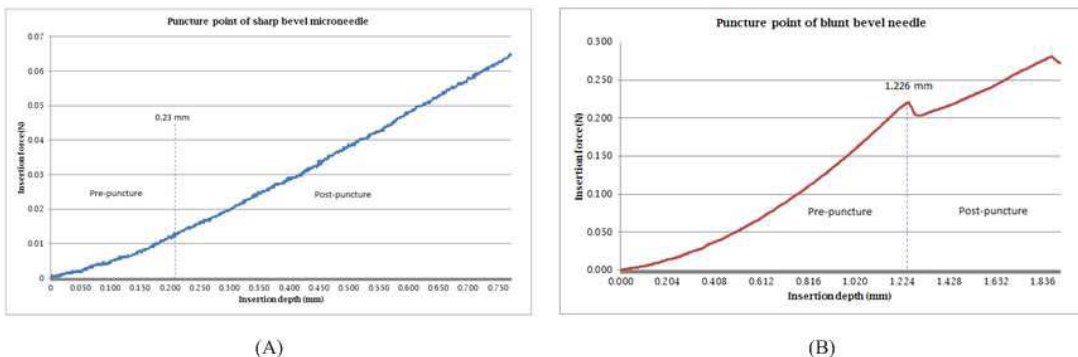


Fig. 21: Puncture point of (A) sharp bevel microneedle and (B) blunt bevel microneedle.

To evaluate our developed post-puncture force modeling, we conducted simulations of using the solid needles of sharp bevel, blunt bevel, and cylindrical needle shapes inserting on the silicone rubber material in the experiments. Fig. 22 shows the result data obtained from the experiments conducted and the simulations results based on the presented analytical models. Fig. 22 shows the comparison between the computed and experimental data of sharp bevel microneedle. The presented algorithm is able to approximate the post-puncture function of the sharp bevel microneedle quite reasonably well. To model the relationship of the adhesion force and cutting area, more experiment on various tip angles may be needed.

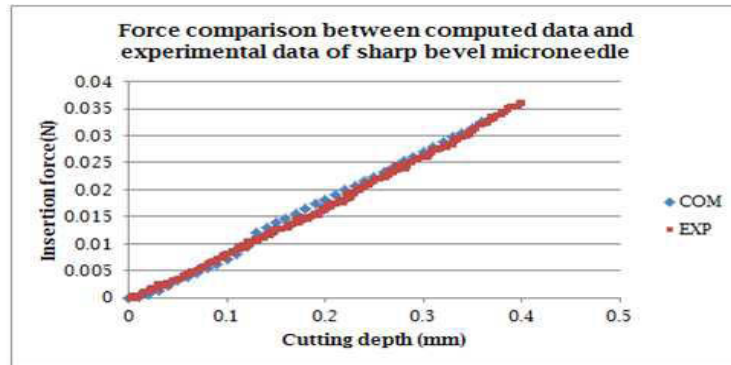


Fig. 22: Comparison of experimental and simulation results of the insertion force and cutting depth by a sharp bevel microneedle at  $S = 0.168$ .

## 5 CONCLUSIONS

In this paper, a nonlinear analytical modeling and a method of solving the nonlinear modeling have been presented to analyze the microneedle insertion force and to evaluate different microneedle geometries. To analyze the microneedle insertion force, monotonous and heterogeneous tetrahedral models of soft tissue were developed. A two-stage analytical modeling technique is presented to evaluate different microneedle designs by considering different geometric design parameters. The presented method divides microneedle insertion process into pre-puncture and post-puncture stages, and employs the concept of finite element analysis, fracture mechanics and distributed load. Our method follows the mechanics of microneedle insertion and keeps monitoring the changes in forces and soft tissue deformation. Once the energy equation derived using fracture mechanic is balanced, the puncture point is reached and recorded. The insertion force during the post-puncture is lastly computed based on distributed load and computational geometry method. Computer algorithm implementation results and the laboratory experiment results were presented in this paper. The analytic modeling discussed in this paper can be used to analyze and evaluate the different possible microneedle geometric designs. The presented techniques can be used for the design and development of microneedle apparatus for biomedical applications.

## 6 ACKNOWLEDGEMENT

This work was partially supported by the National Science Foundation (NSF) Grants (CMMI- 0800811, CMMI- 1125872). Their support is greatly appreciated. We are also grateful for the assistance of P. Wongwiwat and R. Boehm in the laboratory experiments.

## 7. REFERENCES

- [1] Kim, E.; Narayan, R.; and Lee, Y.- S.: Analytical Modeling And Excimer Laser Micromachining of Microchannel For Medical Devices Development, Proceedings of 2010 ASME International Mechanical Engineering Conference and Exhibition (IMECE), Vancouver, BC, Canada, November 12- 18, 2010, (CD) Paper Number: IMECE2010- 40985.
- [2] Park, J.- H.; Allen, M. G.; Prausnitz, M. R.: Biodegradable polymer microneedles: Fabrication, mechanics and transdermal drug delivery. *Journal of Controlled Release*, no. 104, 2005, 51- 66. DOI:10.1016/j.jconrel.2005.02.002.
- [3] Park, J.- H.; Yoon, Y.- L.; Choi, S.- O.; Prausnitz, M. R.; Allen, M. G.: Taper conical polymer microneedles fabricated using an integrated lens technique for transdermal drug delivery. *IEEE Transactions on Biomedical Engineering*, 54(5), 2007, 903–913. DOI: 10.1109/TBME.2006.889173.
- [4] Doran, C. F.; McCormack, B. A. O.; Macey, A.: A simplified model to determine the contribution of strain energy in the failure process of thin biological membranes during cutting. *Strain*, no. 40, 2004, 173- 179. DOI: 10.1111/j.1475- 1305.2004.tb01426.x
- [5] He, X.; Chen, Y.; Libo, T: Haptic Simulation of Flexible Needle Insertion. Proceedings of the 2007 IEEE International Conference on Robotics and Biomimetics, Sanya, China, 2007, 607- 611. DOI: 10.1109/ROBIO.2007.4522231.
- [6] Zahn, J. D.; Talbot, N. H.; Dorian, L.; Pisano, P.: Micro- fabricated polysilicon microneedles for minimally invasive biomedical devices, *Biomed. Microdevices* 2, 2000, 295 – 303. DOI: 10.1023/A:1009907306184.
- [7] Davis, S. P.; Landis, B. J.; Adams, Z. H.; Allen, M. G.; Prausnitz, M. R.: Insertion of microneedles into skin: measurement and prediction of insertion force and needle fracture force. *Journal of Biomech.* 37, 2004, 1155- 1163. DOI:10.1016/j.jbiomech.2003.12.010
- [8] Azar, T.; and Vincent, H.: Estimation of the fracture toughness of soft tissue from needle insertion. *Proceeding of Biomedical Simulation, 4th International Symposium, ISBMS 2008, Lecture Notes in Computer Science. Springer Verlag, 2008, 166- 175. DOI: 10.1007/978- 3- 540- 70521- 5\_18*
- [9] Lin, S. Y.; Narayan, R.; Lee, Y.- S.: Heterogeneous Deformable Modeling and Topology Modification for Surgical Cutting Simulation with Haptic Interfaces, *Computer- Aided Design and Application*, 5(6), 2008, 877- 888. doi:10.3722/cadaps.2008.877- 888.
- [10] Ko, K. W.; Kim, H.; Bae, S.; Kim, E.; Lee, Y.- S.: Determination of Spring Constant for Simulating Deformable Object under Compression, *Journal of Key Engineering Materials*, 417- 418(2), 2010, 369- 372. DOI: 10.4028/www.scientific.net/KEM.417- 418.369.
- [11] Timoshenko, S. P.; Gere J. M.: *Theory of Elastic Stability.* McGRAW- Hill Book Company, INC., New York, 1961.
- [12] Odland, G: *Structure of the skin, In Physiology, biochemistry and molecular biology of the skin,* Oxford University Press, Oxford, 1991.
- [13] Conn, N.; Gould, N.; Toint, P.: *Trust- Region Methods.* MPS/SIAM Series on Optimization, SIAM and MPS 2000.
- [14] Pailler- Matteri, C.; Pavan, S.; Vargiolu, R.; Pirot, F.; Falson, F.; Zahouani, H.: Contribution of

- stratum corneum in determining bio- triological properties of the human skin. *Wear* 263, 2007, 1038 – 1043. DOI:10.1016/j.wear.2007.01.128.
- [15] L' Etang, A.; Huang, Z.: FE simulation of laser generated surface acoustic wave propagation in skin. *Ultrasonics* 44, 2006, 1243 – 1247. DOI:10.1016/j.ultras.2006.05.077.
- [16] Geuzaine C.; Remacle J.- F.: Gmsh: a three dimensional finite element mesh generator with built-in pre- and post- processing facilities. 2010. [www.geuz.org/gmsh/](http://www.geuz.org/gmsh/)
- [17] Maurin, B.; Barbe, L.; Bayle, B.; Zanne, P.; Gangloff, J.; De Mathelin, M.; Gangi, A.; Soler, L.; Forgione, A.: In vivo study of forces during needle insertions. Proceeding of the medical robotics, navigation and visualisation scientific workshop 2004. DOI: 10.1142/9789812702678\_0056.